Allocating dissipation across a molecular machine cycle to maximize flux

Aidan I. Brown[a] and David A. Sivak[a,1]

[a]Department of Physics, Simon Fraser University, Burnaby, BC, Canada V5A1S6

Biomolecular machines consume free energy to break symmetry and make directed progress. Nonequilibrium ATP concentrations are the typical free energy source, with one cycle of a molecular machine consuming a certain number of ATP, providing a fixed free energy budget. Since evolution is expected to favor rapid-turnover machines that operate efficiently, we investigate how this free energy budget can be allocated to maximize flux. Unconstrained optimization eliminates intermediate metastable states, indicating that flux is enhanced in molecular machines with fewer states. When maintaining a set number of states, we show that—in contrast to previous findings—the flux-maximizing allocation of dissipation is not even. This result is consistent with the coexistence of both "irreversible" and reversible transitions in molecular machine models that successfully describe experimental data, which suggests that, in evolved machines, different transitions differ significantly in their dissipation.

molecular machines | nonequilibrium steady state | dissipation

Biomolecular machines, typically composed of protein complexes, perform many roles inside cells, including cargo transport and energy conversion (1). These microscopic machines operate stochastically (2) but must, on average, make forward progress to fulfill their cellular roles, a functional requirement that, according to the Second Law, imposes a free energy cost (3).

Biomolecular machines typically make use of the free energy stored in nonequilibrium chemical concentrations, which are, in turn, maintained by other cellular machinery (4). The free energy consumed over a forward machine cycle equals the free energy difference between the chemical reactants and products (5), which sets the maximum available dissipation "budget" for a cycle.

Theoretical studies have found that, under a variety of criteria, an even allocation of dissipation across all transitions in a machine cycle is optimal (6–15). However, many models parametrized to experimental biomolecular machine dynamics contain effectively irreversible transitions (16–22), suggesting that some transitions dissipate a large amount of free energy compared with the "reversible" transitions in the same cycle.

The dissipation allocation generally affects the probability flux (also known as the current) through a molecular machine cycle (23). Flux reports on the machine output and thus is an important operating characteristic; indeed, the dependence of flux on alternative energy landscapes was recently proposed to explain the ubiquity of the rotary mechanism of ATP synthase (13).

We approximate molecular machine dynamics with stochastic transitions between discrete states (1, 24) and examine how a fixed free energy dissipation budget should be allocated to a cycle's individual transitions to achieve maximal flux. We find that, without additional constraints, maximizing the flux effectively eliminates the free energy wells representing intermediate metastable states. When constrained to maintain a set number of intermediate metastable states, our central result is that flux is maximized when dissipation is unevenly allocated among the distinct cycle transitions.

Our result is consistent with the presence in the same cycle of both reversible and effectively irreversible transitions and the substantially different implied dissipations (16–22). This suggests that understanding how forward progress is affected by a dissipation allocation may be useful for evaluating the design of biomolecular machines. Adjustment of the dissipation allocation of a biomolecular machine may be relatively easy to parsimoniously achieve compared with broad-reaching changes, such as to the fuel source or to the free energy of ATP hydrolysis.

Models

Discrete States. We consider two- and three-state cycles (Fig. 1), which have frequently been used to model driven in vivo systems, such as myosin (25), kinesin (16), phosphorylation–dephosphorylation cycles (26), the canonical Michaelis–Menten scheme (5), and various specific enzymes (26, 27). For the two-state Michaelis–Menten scheme (5), the first transition binds the substrate, while the second catalyzes the reaction of substrate to product, releases the product, and returns the enzyme to its original state. For a three-state kinesin model (16), the first transition binds ATP to the microtubule-bound head, the second steps the free head forward to bind the microtubule and release ADP, and the third hydrolyzes ATP and unbinds the newly rear head from the microtubule.

In our model cycle, for every forward rate constant k_{ij}^+ describing transitions from state i to state j, there is a nonzero reverse rate constant k_{ij}^- describing transitions from state j to state i. Although some models of molecular machines describe certain transitions as "irreversible," with a reverse rate of zero, this violates the principle of microscopic reversibility (23, 28).

A transition from state i to state j occurs at the forward rate $k_{ij}^+ P_i$, with P_i being the probability in state i. Reverse transitions

---

Significance

Cells use molecular machines to complete many tasks. These machines consume free energy to operate, typically by converting a high-concentration chemical into a low-concentration one. Each step of a machine's operating cycle consumes some free energy, and different allocations of the available free energy among the machine steps lead to different machine speeds. We show that the speed-maximizing allocation is not even, instead depending on the timescales of the various steps. Models fit to experimental molecular machine dynamics often find similarly uneven free energy use. Deviations from the optimal allocation can drastically slow machine operation, suggesting a significant functional advantage to machines with dissipation allocation that is tuned to improve speed.
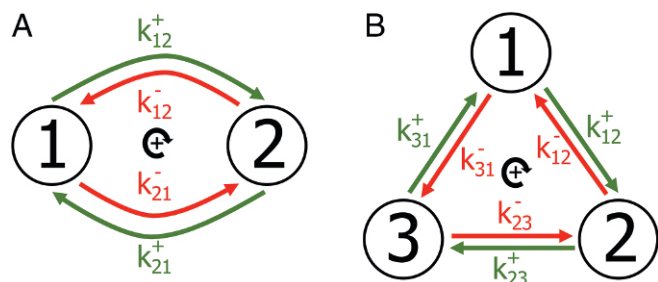
Fig. 1. Small discrete-state cycles. (*A*) Two-state and (*B*) three-state cycles. Forward (clockwise; green) and reverse (counterclockwise; red) transitions occur along each pathway connecting two states, with rate constants k_{ij}^+ and k_{ij}^-, respectively.

from state j to state i occur at rate $k_{ij}^- P_j$. (Note that the two-state cycle has both pathway 12 and pathway 21, representing distinguishable physical transition mechanisms, each with a forward direction and a reverse direction.)

Typically, cellular cycles are driven by nonequilibrium concentrations of reacting chemical species, most prominently ATP, ADP, and inorganic phosphate (P_i) (5). The free energy ΔG provided by ATP hydrolysis depends on the respective concentrations (5),

$$\Delta G = \Delta G_0 + k_B T \ln \frac{[ADP][P_i]}{[ATP]}, \qquad [1]$$

where $\Delta G_0 \equiv -k_B T \ln\left([ADP]_{eq}[P_i]_{eq}/[ATP]_{eq}\right)$, k_B is Boltzmann's constant, and T is the temperature of the surrounding environment. Under physiological conditions, hydrolysis of ATP to ADP and P_i provides free energy $|\Delta G| \sim 20 k_B T$ (5). From here on, we set $k_B T = 1$—all free energies are in units of the thermal energy scale.

The ratio between the forward and reverse rate constants of a given transition path is fixed by its free energy dissipation ω_{ij} (29, 30):

$$\omega_{ij} = \ln \frac{k_{ij}^+}{k_{ij}^-}. \qquad [2]$$

(Additional information is in *SI Appendix*.) Without a bias ω_{ij}, the full forward and reverse rate constants $k_{ij}^{+/-}$ equal the "bare" rate constants k_{ij}^0.

Free Energy Landscape. A discrete-state kinetic model of a machine cycle can also be equivalently represented by Arrhenius dynamics on a free energy landscape, with each free energy well representing a discrete state and the free energy differences between barriers (at energies $E_{ij}^\ddagger$) and states (at energies E_i) determining the rate constants:

$$k_{ij}^+ = \tau_{ij}^{-1} e^{-(E_{ij}^\ddagger - E_i)} \text{ and } k_{ij}^- = \tau_{ij}^{-1} e^{-(E_{ij}^\ddagger - E_j)}, \qquad [3]$$

with τ_{ij} being a timescale accounting for effective diffusivity. The free energy budget ω_{tot} fixes the free energy difference between equivalent molecular machine states separated by one cycle. For example, Fig. 2 represents a two-state cycle, with dissipations $\omega_{12} = E_1 - E_2$ and $\omega_{21} = E_2 - (E_1 - \omega_{tot})$.

The bare rates k_{ij}^0 are the rates in the absence of chemical driving. We restrict our attention to wells at equal free energy without chemical driving, and therefore, forward and reverse bare rates of a given transition are equal. We allow bare rates to vary among the different transitions to account for differences in barrier heights, effective diffusivity, and all other dissipation-independent factors.

Results

We maximize the steady-state flux by allocating a fixed free energy budget ω_{tot} among the free energy differences ω_{ij} between discrete states (i.e., dissipation over discrete transitions) that determines the full rate constants $k_{ij}^{+/-}$ and hence the net steady-state flux J (from here on, the flux), which for a two-state cycle, is (31)

$$J = \frac{k_{12}^+ k_{21}^+ - k_{12}^- k_{21}^-}{k_{12}^+ + k_{12}^- + k_{21}^+ + k_{21}^-}. \qquad [4]$$

We first consider freely varying E_2, $E_{12}^\ddagger$, and $E_{21}^\ddagger$ (Fig. 2). When barriers are higher than states, decreasing the barrier energies always increases flux:

$$\frac{\partial J}{\partial E_{12}^\ddagger} < 0 \text{ and } \frac{\partial J}{\partial E_{21}^\ddagger} < 0. \qquad [5]$$

(Details are in *SI Appendix*.) Flux is maximized when the "barriers" are at or below the states and thus are no longer acting as barriers. This is an intuitive result that, all else equal, faster transitions (because of lowered barriers) produce a higher flux (29).

Increasing E_2 is equivalent to decreasing the dissipation ω_{12}, increasing ω_{21}, and vice versa. For fixed barrier energies $E_{12}^\ddagger$ and $E_{21}^\ddagger$, flux is maximized by increasing E_2 above the free energy of one of the barriers, effectively producing a one-state cycle (*SI Appendix*).

Transition rates are reduced by energetic barriers, and therefore, flux is maximized by removing barriers and reducing the number of metastable states. However, a greater number of metastable states, each representing a persistent conformation or ligand binding status of a biomolecular machine, make possible a larger array of schemes for the following: interaction, such as distinct binding affinities (32); machine operation, such as "gating" (33); and regulation through variable action on distinct states (34).

Multiple metastable states can be maintained by constraining the free energy landscape to preserve barriers. We implement these constraints by fixing the free energy differences between wells and either the barriers immediately before or immediately after them, equivalent to fixing the rate constants between discrete states for either the forward or reverse transitions. A forward labile (FL) scheme (case A in ref. 35) keeps the reverse free energy differences fixed, with the dissipation ω_{ij} only modifying the forward rate constant:

$$k_{ij}^+ = k_{ij}^0 e^{\omega_{ij}} \text{ and } k_{ij}^- = k_{ij}^0; \qquad [6]$$

however, for a reverse labile (RL) scheme (case B in ref. 35), the dissipation only modifies the reverse rate constant:
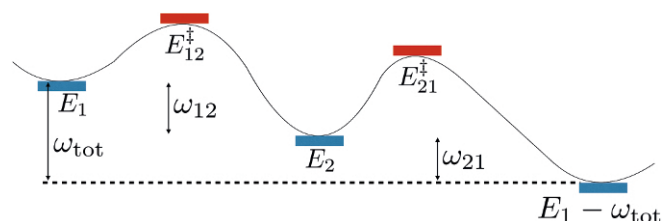

Fig. 2. Free energy landscape representing a two-state molecular machine. The leftmost state (at free energy E_1) and the rightmost state ($E_1 - \omega_{tot}$) represent the same stage of molecular machine operation separated by one complete cycle. The middle state (E_2) represents an intermediate state, while $E_{12}^\ddagger$ and $E_{21}^\ddagger$ are the free energies of barriers between the states. ω_{12} and ω_{21} are the dissipations for each transition, which sum to ω_{tot}, the dissipation budget for one cycle.

$$k_{ij}^+ = k_{ij}^0 \quad \text{and} \quad k_{ij}^- = k_{ij}^0 e^{-\omega_{ij}}. \tag{7}$$

For the free energy landscape of Fig. 2, the FL scheme has fixed $E_{12}^\ddagger - E_2$ and $E_{21}^\ddagger - (E_1 - \omega_{\text{tot}})$, while the RL scheme has fixed $E_{12}^\ddagger - E_1$ and $E_{21}^\ddagger - E_2$.

"Labile" here denotes the direction in which rate constants change with dissipation. This dependence of forward or reverse rate constants on dissipation for the FL and RL schemes, respectively, is analogous to their dependence on the work performed by a motor in a "power stroke" or "Brownian ratchet" (29).

FL Scheme.

Two-state cycle. For a two-state FL cycle (Fig. 1*A*) with fixed total cycle dissipation $\omega_{\text{tot}} = \omega_{12} + \omega_{21}$, flux (Eq. **4**) is maximized when the free energy dissipation of the first transition is

$$\omega_{12}^* = \frac{1}{2}\omega_{\text{tot}} + \frac{1}{2}\ln\frac{k_{21}^0}{k_{12}^0}. \tag{8}$$

This produces equal forward rate constants,

$$k_{ij}^+ = \sqrt{k_{12}^0 k_{21}^0}\; e^{\frac{\omega_{\text{tot}}}{2}}, \tag{9}$$

equal to the geometric mean of any full rate constants k_{12}^+ and k_{21}^+ consistent with the bare rate constants k_{ij}^0 and total dissipation ω_{tot}.

The optimal allocation of total dissipation ω_{tot} differs from the "naïve" allocation $\frac{1}{2}\omega_{\text{tot}}$ that evenly divides the dissipation among the transitions. More specifically, the optimal deviation from the naive allocation is $\Delta\omega_{12}^* \equiv \omega_{12}^* - \frac{1}{2}\omega_{\text{tot}} = \frac{1}{2}\ln(k_{21}^0/k_{12}^0)$. The optimal allocation compensates for variation in bare rate constants, and therefore, for FL, transitions with larger k_{ij}^0 are optimally allocated less dissipation. In fact, the optimal allocation of dissipation to one transition is negative when $|\ln(k_{21}^0/k_{12}^0)| > \omega_{\text{tot}}$.

Three-state cycle. For a three-state cycle (Fig. 1*B*), the flux is (31)

$$J = \frac{k_{12}^+ k_{23}^+ k_{31}^+ - k_{12}^- k_{23}^- k_{31}^-}{\left(\begin{array}{c} k_{12}^+ k_{23}^- + k_{12}^- k_{23}^- + k_{23}^- k_{31}^- + k_{12}^+ k_{31}^+ + k_{12}^- k_{31}^+ \\ + k_{12}^- k_{31}^- + k_{12}^+ k_{23}^+ + k_{23}^+ k_{31}^+ + k_{23}^- k_{31}^- \end{array}\right)}. \tag{10}$$

For FL, Fig. 3 shows the numerically determined allocation of free energy dissipation that maximizes the flux subject to a fixed $\omega_{\text{tot}} = \omega_{12} + \omega_{23} + \omega_{31}$ and fixed second and third bare rate constants $k_{23}^0 = k_{31}^0 = 1$ for several different k_{12}^0 across multiple orders of magnitude (27). When $k_{12}^0 = 1$, the ω_{ij}^* all equal the naive value $\frac{1}{3}\omega_{\text{tot}}$ as expected by symmetry. As k_{12}^0 increases, the optimal allocations ω_{ij}^* depart from the naive case, with the dissipation ω_{12}^* of the first transition decreasing and that of the second and third transitions (ω_{23}^* and ω_{31}^*) increasing.

At high ω_{tot}, the reverse flux is much smaller than the forward flux, $J_{ij-} = k_{ij}^- P_j \ll k_{ij}^+ P_i = J_{ij+}$, and hence, the net flux roughly equals the forward flux, $J = J_{ij+} - J_{ij-} \simeq J_{ij+}$. In this limit, the cycle effectively only has forward transitions, leading (*SI Appendix*) to an optimal dissipation allocation

$$\Delta\omega_{12}^* = \frac{1}{3}\ln\frac{k_{23}^0 k_{31}^0}{(k_{12}^0)^2} \tag{11}$$

that is independent of ω_{tot}. Similar expressions for $\Delta\omega_{23}^*$ and $\Delta\omega_{31}^*$ are found by cyclically permuting the indices in Eq. **11**. These asymptotic values (Fig. 3, circles on the right edge) are indistinguishable from the limits of the numerical calculations. This optimal dissipation allocation produces equal forward rate constants

$$k_{ij}^+ = k_{ij}^0 e^{\omega_{ij}} = (k_{12}^0 k_{23}^0 k_{31}^0 e^{\omega_{\text{tot}}})^{\frac{1}{3}} \tag{12}$$

that are the geometric mean of any full rate constants k_{12}^+, k_{23}^+, and k_{31}^+, consistent with k_{ij}^0 and ω_{tot}.
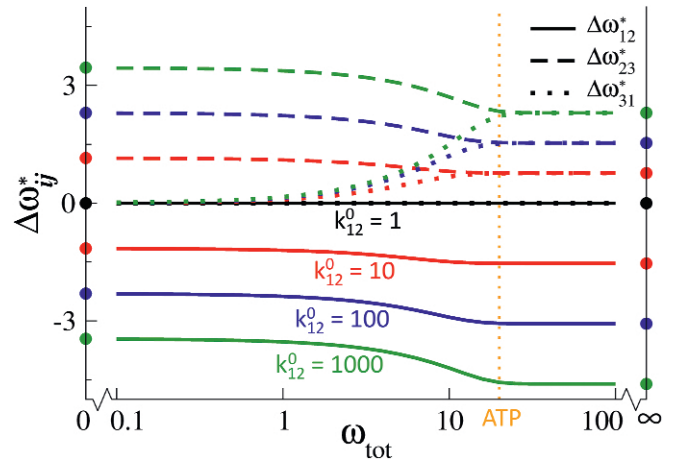

Fig. 3. Uneven allocation of dissipation maximizes flux in a three-state FL cycle. Dissipation allocations $\Delta\omega_{12}^*$ (solid curves), $\Delta\omega_{23}^*$ (dashed), and $\Delta\omega_{31}^*$ (dotted) for the three transitions in Fig. 1*B* that maximize the flux. Dissipations are expressed as differences $\Delta\omega_{ij}^* \equiv \omega_{ij}^* - \frac{1}{3}\omega_{\text{tot}}$ from the naive allocation of equal dissipation $\frac{1}{3}\omega_{\text{tot}}$ to each transition. $k_{23}^0 = k_{31}^0 = 1$ is fixed, and k_{12}^0 varies with color. When $k_{12}^0 = 1$ (black), an even allocation of dissipation to each transition maximizes flux, and therefore, $\Delta\omega_{ij}^* = 0$ for all ω_{tot}. As k_{12}^0 increases (black → red → blue → green), the flux-maximizing allocation increasingly deviates from an even allocation as shown by the increasing magnitude of $\Delta\omega_{ij}^*$. Allocations at limiting ω_{tot} are shown by circles [low ω_{tot} plotted at $\omega_{\text{tot}} = 0$ (Eq. **11**); high ω_{tot} at $\omega_{\text{tot}} = \infty$ (Eq. **13**)]. The vertical dotted orange line at $\omega_{\text{tot}} = 20$ represents the ATP hydrolysis free energy under physiological conditions.

At low ω_{tot}, when the net flux $J = J_{ij+} - J_{ij-}$ is much smaller than either the forward or reverse fluxes $J \ll J_{ij+}$ and $J \ll J_{ij-}$, the optimal ω_{ij} also asymptotically approaches (generally nonzero) values independent of ω_{tot}. Maximizing the net flux in Eq. **10** at low ω_{tot} leads (*SI Appendix*) to an optimal allocation

$$\omega_{12}^* = \frac{1}{2}\ln\frac{k_{31}^0}{k_{12}^0}. \tag{13}$$

Similar expressions for ω_{23}^* and ω_{31}^* are found by cyclically permuting the indices in Eq. **13**. These asymptotic values (Fig. 3, circles on the left edge) show excellent agreement with the limiting numerical calculations.

At high total dissipation ω_{tot}, the optimal allocation ω_{ij}^* reaches a limit where, for all transitions, the forward rates are much larger than the reverse rates, becoming effectively irreversible. For the three-state cycle, the 20 $k_{\text{B}}T$ of free energy provided by ATP hydrolysis is near this limit (Fig. 3). However, not all transitions will be effectively irreversible for a smaller dissipation budget per cycle step, which is obtained for machines that perform work against a resistive load or machines with more states per cycle.

The results above show that the optimal allocation of dissipation can significantly differ from an equal allocation to each transition. Fig. 4 shows the variation of flux as the dissipation allocation is varied away from the optimal allocation. Exploring a range of several $k_{\text{B}}T$ around the optimal allocation, the flux varies by more than three orders of magnitude. Thus, a dissipation allocation significantly different from the optimal one can qualitatively alter the cycle output.

RL Scheme.
For a two-state RL cycle (as opposed to an FL cycle), the flux-maximizing allocation of dissipation is (*SI Appendix*)

$$\Delta\omega_{12}^* = -\frac{1}{2}\ln\frac{k_{21}^0}{k_{12}^0}. \tag{14}$$
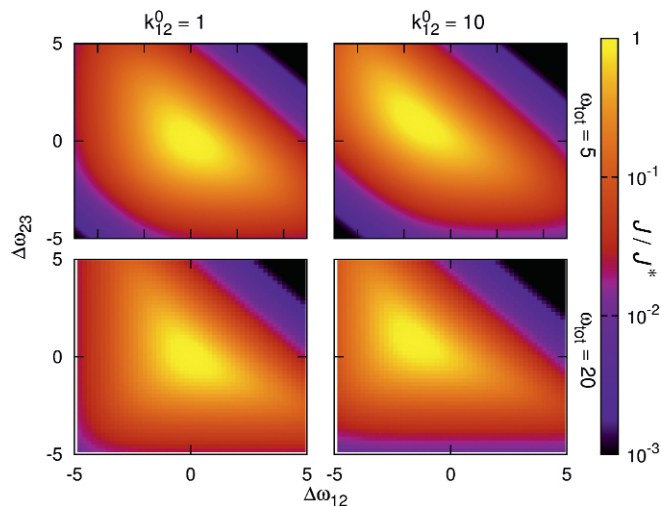
Fig. 4. Flux is sensitive to dissipation allocation. Flux ratio J/J^* as a function of the dissipation allocation for the three-state FL cycle with $k_{23}^0 = k_{31}^0 = 1$ and k_{12}^0 and ω_{tot} varying across subplots. Dissipation allocations are shown as differences $\Delta\omega_{ij} \equiv \omega_{ij} - \frac{1}{3}\omega_{tot}$ from naive values $\frac{1}{3}\omega_{tot}$. Optimal flux J^* is specific to each subplot.

The deviations in Eq. **14** from naive allocations are identical to the FL result [**8**], except assigned to the other transition. Despite this apparent difference, in each state, the probability that the next transition will move in the forward or reverse direction (and hence, the ratio of one-sided fluxes) is identical for the optimized FL and RL cycles. For example, both schemes produce one-sided fluxes departing from state 1 that satisfy (*SI Appendix*)

$$\frac{J_{12+}^*}{J_{21-}^*} = \sqrt{\frac{k_{12}^0}{k_{21}^0}} e^{\frac{\omega_{tot}}{2}}. \qquad [15]$$

Similarly, for the three-state cycle, both mechanisms allocate dissipation identically, except cyclically permuted (Fig. 5*A*). Thus, optimal dissipation allocation in the three-state cycle also produces one-sided flux ratios that do not depend on the mechanism. The limiting optimal allocations at high ω_{tot} are (*SI Appendix*)

$$\Delta\omega_{12}^* = \frac{1}{3}\ln\frac{k_{12}^0 k_{31}^0}{\left(k_{23}^0\right)^2}, \qquad [16]$$

and at low ω_{tot}, they are (*SI Appendix*)

$$\omega_{12}^* = \frac{1}{2}\ln\frac{k_{12}^0}{k_{23}^0}. \qquad [17]$$

These results are intuitive: an RL scheme can adjust reverse but not forward rates, and therefore, to maximize the flux, it allocates more dissipation to decelerate the fastest reverse rates (those with high k_{ij}^0); however, an FL scheme can adjust forward but not reverse rates, and therefore, it allocates more dissipation to accelerate the slowest forward rates (with low k_{ij}^0).

Fig. 5*B* shows the dependence of three-state RL flux on the dissipation allocation. For low ω_{tot}, the flux varies substantially (by orders of magnitude) across allocations that differ by a few $k_B T$ (similar to FL in Fig. 4), but at high ω_{tot}, there is little variation of flux with dissipation allocation. The RL flux is less sensitive to the dissipation allocation at high ω_{tot}, because after reverse rates are sufficiently suppressed to be negligible (i.e., for $e^{-\omega_{tot}/3} \ll 1$), reallocation of dissipation has reduced effect.

For given bare rates k_{ij}^0 and total dissipation ω_{tot}, an FL cycle will always produce more flux than the corresponding RL cycle,

similar to previous results (29). FL and RL schemes represent extremes of a more general mechanism, whereby some dissipation is spent speeding up the forward transitions (as for FL), and the remaining fraction slows down the reverse transitions (as for RL):

$$k_{ij}^+ = k_{ij}^0 e^{\omega_{ij}^+} \quad \text{and} \quad k_{ij}^- = k_{ij}^0 e^{-\omega_{ij}^-}. \qquad [18]$$

This is similar to splitting force dependence among reaction rates in previous studies (28, 29). $\sum(\omega_{ij}^+ + \omega_{ij}^-) = \omega_{tot}$ is fixed, leaving $2n - 1$ free parameters to optimize over in an n-state cycle. For any given dissipation allocation, flux can always be increased by shifting some dissipation $\delta\omega$ from slowing the reverse rate to speeding the corresponding forward rate. This is equivalent to simply lowering the barriers for the free energy landscape in Fig. 2, which removes the distinction between states as discussed above.

Discussion

The Second Law of thermodynamics requires free energy dissipation to break detailed balance and maintain directed flux (3) but does not specify a quantitative relationship between dissipation and flux (14, 36, 37).

From the perspective of a free energy landscape, we find that the flux is increased by lowering the barriers, so that they are no longer effective. This is intuitive, as transition rates are reduced by energetic barriers, and it suggests that molecular
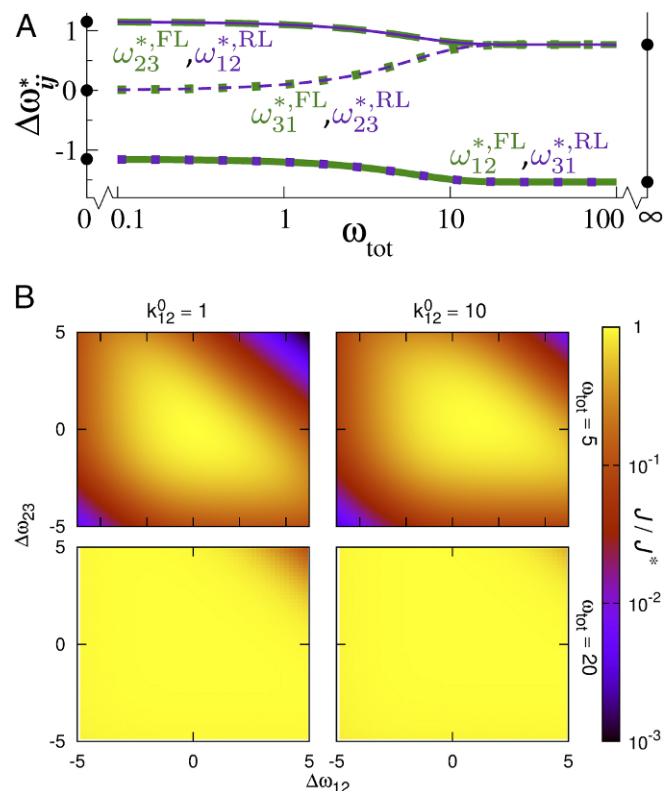

Fig. 5. Optimal and suboptimal allocations of dissipation for RL scheme. (*A*) Allocation of dissipation ω_{ij} to maximize flux around the three-state cycle for FL (green) and RL (purple) schemes. The optimal dissipation values are identical for the two mechanisms (as illustrated by the overlapping green and purple curves on the plot); however, the individual dissipations are allocated to different transitions. Circles on the left and right edges show limiting optimal allocations at low (Eq. **17**) and high total dissipation ω_{tot} (Eq. **16**), respectively. $k_{12}^0 = 10$, and $k_{23}^0 = k_{31}^0 = 1$. (*B*) Flux sensitivity to dissipation allocation, analogous to Fig. 4, except for RL scheme instead of FL.
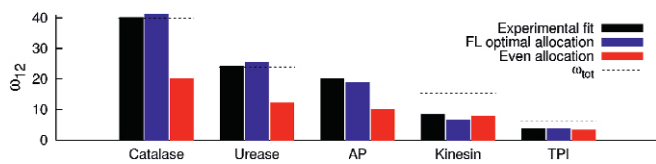
Fig. 6. FL predictions better match experimental dissipation allocations than do even allocations. Dissipation of transition ω_{12} in several enzymes from fit to experiment (black) (27), flux optimization under the FL scheme (blue), and even allocation (red). Details are in *SI Appendix*. AP, alkaline phosphatase; TPI, triose phosphate isomerase.

machines should reduce the number of metastable states to increase forward flux. However, molecular machines perform their tasks using multiple metastable states, and accordingly, we have focused on scenarios that allow distinct states to be maintained.

In a reaction cycle with a fixed number of discrete states, we have shown that flux is maximized by an uneven allocation of a fixed dissipation budget among the various discrete transitions, compensating for differences in the bare rate constants of each transition (Eqs. **8** and **14** and Figs. 3 and 5*A*). This is related to recent findings that flux is affected differently by adjusting the bare rate of different transitions (29). The flux can be quite sensitive to the precise dissipation allocation (Figs. 4 and 5*B*), suggesting a significant cost to nonoptimal allocations.

This result differs from the uniform allocations found to be optimal in various other contexts, including maximizing power at fixed entropy production rate (6), minimizing entropy production at fixed flux (7–9), maximizing free energy conversion efficiency (10), and minimizing the dissipation cost of a given precision (14). Several other studies have argued that, to maintain a high flux, large free energy increases should be broken up into smaller pieces, with no individual free energy change too large (11–13). Even in synthetic molecular motors, it is thought that similar forward rates are optimal (to avoid "traffic jams") (15).

We find that an unequal optimal dissipation allocation occurs when: the nonequilibrium steady-state flux is maximized; optimization is subject to fixed total dissipation budget per cycle; the ratio of forward and reverse rate constants varies exponentially, not linearly, with dissipation (Eq. **2**); and cycle transitions have different bare rate constants, corresponding to different barrier heights and effective diffusivities. For some previous studies finding even dissipation allocations to be optimal, a single change is sufficient to make uneven allocations optimal [e.g., imposing distinct bare rate constants (14) or changing the dependence of flux on dissipation from linear (the near-equilibrium case) to exponential (8)].

Many models parametrized to biomolecular machine dynamics contain effectively irreversible transitions [e.g., models of kinesin (16, 17), myosin (18, 19), RNA polymerase (20), and viral packaging motors (21, 22)]. Such irreversible transitions are, strictly speaking, unphysical because of their violation of microscopic reversibility (23, 28); in reality, they represent a forward rate constant much larger than the reverse rate constant, a signature of large dissipation over that transition. Since other transitions in these models are reversible, this implies that the dissipation allocation in such models must be highly unequal, consistent with the uneven dissipation allocation that we find maximizes flux.

Other models of driven biomolecular cycles—such as in myosin (38–40) and several enzymes (27)—lack explicitly irreversible transitions but have ratios of forward and reverse rate constants, and hence, free energy dissipation, that vary significantly across the different reactions composing a cycle.

Dissipation biases forward and reverse rate constants, but there is no unique way to achieve this bias (29, 35). We explored in detail two extremes for how dissipation can lead to biased progress: an FL scheme, where dissipation increases forward rate constants; and an RL scheme, where dissipation decreases reverse rate constants. Although FL and RL mechanisms lead to distinct optimal allocations of dissipation, both lead to identical transition probability ratios from each state (Eq. **15**). An FL cycle produces more flux than a comparable RL cycle, but FL flux is quite sensitive to the dissipation allocation (Fig. 4), while RL flux is insensitive to the dissipation allocation for a large free energy budget (Fig. 5*B*).

On evolutionary timescales, mutations alter the conformational free energies of initial and final states differently. For a transition state conformationally similar to the initial state, a mutation should produce similar changes in the initial-state and transition-state free energies, and therefore, the forward rate should change less than the backward rate. This is analogous to the distance to the transition state affecting the sensitivity of unfolding rates to applied force (41). Our FL and RL mechanisms thus correspond to a transition state conformationally similar to the final state and to the initial state, respectively (*SI Appendix*, Fig. S1).

Optimizing an FL cycle predicts that transitions with low bare rate constants will be allocated more dissipation, while for an RL cycle, high bare rate constants are allocated more dissipation. Dissipation allocations for several two-state enzyme models (27) fit to experiment are closely matched by the FL optimal allocation, generally much better than by an even allocation (Fig. 6) or the RL optimal allocation. *SI Appendix* has more extensive comparisons.

We expect that adjusting the dissipation allocation (of a fixed total dissipation per cycle) would require only isolated changes in molecular machine dynamics, primarily affecting machine output or productivity and minimally impacting the rest of the cell. In contrast, adjusting the dissipation budget (for example, through the free energy of ATP hydrolysis) would affect numerous driven processes throughout the cell.

Adjustment of the dissipation allocation through isolated mutations is supported by experimental findings. Point mutations in the kinesin-1 nucleotide binding pocket likely affect the dissipation allocation by altering the size of the pocket (42) or the ADP unbinding rate (43, 44) and lead to significant decreases in kinesin velocity or ATP hydrolysis rate while remaining functional. Changes in binding affinity caused by mutation [e.g., 2.5-fold change for a transcription regulator (45) or 40-fold change for a membrane regulatory protein (46)] correspond to a different unbinding rate, which also would change the dissipation allocation.

Our optimizations omit several significant biophysical considerations. For example, we allow rate constants to vary without bound, although practically, they are limited by molecular diffusion. We also focus on a single biomolecular cycle; an interesting extension would be to investigate the effects of alternative pathways thought to be present in biomolecular machines (16, 40). Additional elaborations of this work could explore the sensitivity of flux to (varying) resistive forces as well as cycle states vulnerable to "escape" (such as a molecular motor falling off of its track).

1. Kolomeisky AB (2013) Motor proteins and molecular motors: How to operate machines at the nanoscale. *J Phys Condens Matter* 25:463101.
2. Astumian RD, Bier M (1994) Fluctuation driven ratchets: Molecular motors. *Phys Rev Lett* 72:1766–1769.
3. Machta BB (2015) Dissipation bound for thermodynamic control. *Phys Rev Lett* 115:260603.
4. Boyer PD (1997) The ATP synthase—A splendid molecular machine. *Annu Rev Biochem* 66:717–749.
5. Phillips R, Kondev J, Theriot J, Garcia H (2012) *Physical Biology of the Cell* (Garland Science, New York), 2nd Ed.
6. Qian H, Kjelstrup S, Kolomeisky AB, Bedeaux D (2016) Entropy production in mesoscopic stochastic thermodynamics: Nonequilibrium kinetic cycles driven by chemical potentials, temperatures, and mechanical forces. *J Phys Condens Matter* 28:153004.
7. Qian H (2000) The mathematical theory of molecular motor movement and chemo-mechanical energy transduction. *J Math Chem* 27:219–234.
8. Sauar E, Ratkje SK, Lien KM (1996) Equipartition of forces: A new principle for process design and optimization. *Ind Eng Chem Res* 35:4147–4153.
9. Johannessen E, Kjelstrup S (2005) A highway in state space for reactors with minimum entropy production. *Chem Eng Sci* 60:3347–3361.
10. Oster G, Wang H (2000) Reverse engineering a protein: The mechanochemistry of ATP synthase. *Biochim Biophys Acta Bioenerg* 1458:482–510.
11. Hill T, Eisenberg E (1981) Can free energy transduction be localized at some crucial part of the enzymatic cycle? *Q Rev Biophys* 14:463–511.
12. Yu H, Ma L, Yang Y, Cui Q (2007) Mechanochemical coupling in the myosin motor domain. I. Insights from equilibrium active-site simulations. *PLoS Comput Biol* 3:e21.
13. Anandakrishnan R, Zhang Z, Donovan-Maiye R, Zuckerman DM (2016) Biophysical comparison of ATP synthesis mechanisms shows a kinetic advantage for the rotary process. *Proc Natl Acad Sci USA* 113:11220–11225.
14. Barato AC, Seifert U (2015) Thermodynamic uncertainty relation for biomolecular processes. *Phys Rev Lett* 114:158101.
15. Geertsema EM, van der Molen SJ, Martens M, Feringa BL (2009) Optimizing rotary processes in synthetic molecular motors. *Proc Natl Acad Sci USA* 106:16919–16924.
16. Clancy BE, Behnke-Parks WM, Andreasson JOL, Rosenfeld SS, Block SM (2011) Pathway for kinesin stepping. *Nat Struct Mol Biol* 18:1020–1027.
17. Visscher K, Schnitzer MJ, Block SM (1999) Single kinesin molecules studied with a molecular force clamp. *Nature* 400:184–189.
18. Cappello G, et al. (2007) Myosin V stepping mechanism. *Proc Natl Acad Sci USA* 104:15328–15333.
19. Xie P, Dou SX, Wang PY (2006) Model for kinetics of myosin-V molecular motors. *Biophys Chem* 120:225–236.
20. Abbondanzieri EA, Greenleaf WJ, Shaevitz JW, Landick R, Block SM (2005) Direct observation of base-pair stepping by RNA polymerase. *Nature* 438:460–465.
21. Moffitt JR, et al. (2009) Intersubunit coordination in a homomeric ring ATPase. *Nature* 457:446–450.
22. Liu S, et al. (2014) A viral packaging motor varies its DNA rotation and step size to preserve subunit coordination as the capsid fills. *Cell* 157:702–713.
23. Astumian RD (2015) Irrelevance of the power stroke for the directionality, stopping force, and optimal efficiency of chemically driven molecular machines. *Biophys J* 108:291–303.
24. Keller D, Bustamante C (2000) The mechanochemistry of molecular motors. *Biophys J* 78:541–556.
25. Kolomeisky AB, Fisher ME (2003) A simple kinetic model describes the processivity of myosin-V. *Biophys J* 84:1642–1650.
26. Qian H (2006) Open-system nonequilibrium steady state: Statistical thermodynamics, fluctuations, and chemical oscillations. *J Phys Chem B* 110:15063–15074.
27. Hwang W, Hyeon C (2017) Quantifying the heat dissipation from a molecular motor's transport properties in nonequilibrium steady states. *J Phys Chem Lett* 8:250–256.
28. Fisher ME, Kolomeisky AB (1999) The force exerted by a molecular motor. *Proc Natl Acad Sci USA* 96:6597–6602.
29. Wagoner JA, Dill KA (2016) Molecular motors: Power strokes outperform Brownian ratchets. *J Phys Chem B* 120:6327–6336.
30. Pietzonka P, Barato AC, Seifert U (2016) Universal bound on the efficiency of molecular motors. *J Stat Mech Theory Exp* 2016:124004.
31. Hill T (1977) *Free Energy Transduction in Biology: Steady State Kinetic and Thermodynamic Formalism* (Academic, London).
32. Mason CS, et al. (1999) Serine and tyrosine phosphorylations cooperate in Raf-1, but not B-Raf activation. *EMBO J* 18:2137–2148.
33. Dogan MY, Can S, Cleary FB, Purde V, Yildiz A (2015) Kinesin's front head is gated by the backward orientation of its neck linker. *Cell Rep* 10:1967–1973.
34. Huse M, Kuriyan J (2002) The conformational plasticity of protein kinases. *Cell* 109:275–282.
35. Thomas N, Imafaku Y, Tawada K (2001) Molecular motors: Thermodynamics and the random walk. *Proc R Soc Lond B* 268:2113–2122.
36. Feng EH, Crooks GE (2008) Length of time's arrow. *Phys Rev Lett* 101:090602.
37. Brown AI, Sivak DA (2016) Effective dissipation: Breaking time-reversal symmetry in driven microscopic energy transmission. *Phys Rev E* 94:032137.
38. Fox RF (1998) Rectified Brownian movement in molecular and cellular biology. *Phys Rev E* 57:2177–2203.
39. Skau KI, Hoyle RB, Turner MS (2006) A kinetic model describing the processivity of Myosin-V. *Biophys J* 91:2475–2489.
40. Wu Y, Gao YQ, Karplus M (2007) A kinetic model of coordinated myosin V. *Biochemistry* 46:6318–6330.
41. Elms PJ, Chodera JD, Bustamante C, Marqusee S (2012) The molten globule state is unusually deformable under mechanical force. *Proc Natl Acad Sci USA* 109:3796–3801.
42. Kapoor TM, Mitchison TJ (1999) Allele-specific activators and inhibitors for kinesin. *Proc Natl Acad Sci USA* 96:9106–9111.
43. Higuchi H, Bronner CE, Park HW, Endow SA (2004) Rapid double 8-nm steps by a kinesin mutant. *EMBO J* 23:2993–2999.
44. Uchimura S, Oguchi Y, Hachikubo Y, Ishiwata S, Muto E (2010) Key residues on microtubule responsible for activation of kinesin ATPase. *EMBO J* 29:1167–1175.
45. Huang S, et al. (2016) Structural basis for the selective Pb(II) recognition of metalloregulatory protein PbrR691. *Inorg Chem* 55:12516–12519.
46. Feig LA, Cooper GM (1988) Inhibition of NIH 3T3 cell proliferation by a mutant ras protein with preferential affinity for GDP. *Mol Cell Biol* 8:3235–3243.